Phase knowledge enables rational screens for protein crystallization

Megan J. Anderson*, Carl L. Hansen†, and Stephen R. Quake‡§

*Department of Biochemistry and Molecular Biophysics, California Institute of Technology, MS 128-95, Pasadena, CA 91125; †Departments of Physics and Astronomy and Electrical and Computer Engineering, Michael Smith Laboratories, University of British Columbia, 2185 East Mall, Vancouver, BC, Canada V6T 1Z4; and ‡Department of Bioengineering, Stanford University and Howard Hughes Medical Institute, 318 Campus Drive, Room E300, Stanford, CA 94305

Edited by Stephen L. Mayo, California Institute of Technology, Pasadena, CA, and approved September 21, 2006 (received for review June 23, 2006)

We show that knowledge of the phase behavior of a protein allows one to create a rational screen that increases the success rate of crystallizing challenging proteins. The strategy is based on using microfluidics to perform large numbers of protein solubility experiments across many different chemical conditions to identify reagents for crystallization experiments. Phase diagrams were generated for the identified reagents and used to design customized crystallization screens for every protein. This strategy was applied with a 75% success rate to the crystallization of 12 diverse proteins, most of which failed to crystallize when using traditional techniques. The overall diffraction success rate was 33%, about double what was achieved with conventional automation in large-scale protein structure consortia. The higher diffraction success rates are achieved by designing customized crystallization screens using the phase behavior information for each target. The identification of reagents based on an understanding of protein solubility and the use of phase diagrams in the design of individualized crystallization screens therefore promotes high crystallization rates and the production of diffraction-quality crystals.

microfluidics | protein phase behavior

One of the main bottlenecks in the application of protein crystallography to large-scale structural biology efforts is the production of diffraction-quality crystals. Protein crystallization relies on the identification of reagents that promote crystal formation and an understanding of protein solubility in the presence of these reagents to achieve optimal crystal growth. Traditional techniques to identify reagents for crystallization include incomplete factorial searches across chemical space and sparse-matrix screening around reagents previously shown to crystallize proteins (1, 2). Although these techniques provide a starting point for crystallization experiments, they are not designed around the biophysical properties of individual proteins and have met with limited success for more challenging crystallization targets. For example, the National Institutes of Health Protein Structure Initiative (PSI) was able to generate diffraction-quality crystals from less than one in five of the 10,000 purified protein targets it has attempted to date (http://targetdb.pdb.org/statistics/TargetStatistics.html).

Knowledge of protein solubility in the presence of a crystallizing reagent enables one to effectively use the reagent in a way that will promote crystallization. The traditional method to study protein solubility in response to reagents is to construct a phase diagram that measures the solubility at different protein and reagent concentrations. The protein solubility curve outlined in each phase diagram depicts the most favorable protein and reagent concentrations to use in a crystallization experiment for optimal crystal growth. Currently, phase diagrams are only generated for readily available model proteins and for proteins with known crystallization conditions to improve crystal morphology (3–12). The infrequent use of phase diagrams for crystallization experiments is due to the large sample volumes and time required to construct the diagrams. The general utilization of phase diagrams to analyze protein solubility before starting crystallization experiments would lead to a more physical and rational approach to protein crystallization.

Here, we show that a crystallization strategy based on a detailed understanding of protein solubility increases the crystallization success rate for challenging proteins. A microfluidic formulator device was used to systematically screen hundreds of reagents against protein targets at several points on the phase diagrams to identify reagents that affect the solubility of the protein. Next, each of the identified reagents was explored by constructing a complete phase diagram outlining the solubility limits of the protein in the presence of the reagent. The phase diagrams were then used to design individualized crystallization screens tailored to the solubility properties of the target protein. This device was previously demonstrated to greatly enrich crystallization conditions for xylanase, UMP kinase, and the integral membrane protein SERCA (13, 14). The customized crystallization screens were tested by using a redesigned free interface diffusion screening device. Successful crystallization conditions were transported to a larger-scale crystal growth format for diffraction analysis.

We applied this rational screening strategy to the crystallization of 12 biologically diverse and challenging proteins, 8 of which failed to crystallize when using traditional techniques. The crystallization targets range in size from 16 kDa to 360 kDa complexes and include membrane proteins, large multiprotein complexes, a protein/RNA complex, a metalloprotein complex, metabolic proteins, and an extracellular matrix protein. Identification of reagents and phase diagram generation for each target were completed by using only microliters of sample, and we found that crystallization and diffraction success rates were roughly double that obtained by the PSI when using conventional automation. The increased success rates are noteworthy given the target diversity and that 67% of the targets are from eukaryotic sources while the PSI crystallization targets to date are biased toward prokaryotic sources with only 30% of the targets from eukaryotic sources (http://targetdb.pdb.org/statistics/TargetStatistics.html).

Results and Discussion

The phase diagram-based approach to protein crystallography was used to design and implement customized crystallization strategies for 12 challenging protein targets. To begin, protein solubility was screened against an extensive set of chemical conditions to identify suitable reagents for crystallization trials (Fig. 1*A*). The solubility screening included a full factorial search

Author contributions: M.J.A., C.L.H., and S.R.Q. designed research; M.J.A. performed research; C.L.H. contributed new reagents/analytic tools; M.J.A., C.L.H; and S.R.Q. analyzed data; and M.J.A., C.L.H., and S.R.Q. wrote the paper.

The authors declare no conflict of interest.

This article is a PNAS direct submission.

Abbreviations: MME, modified monomethyl ether; PSI, Protein Structure Initiative.

§To whom correspondence should be addressed. E-mail: quake@stanford.edu.

www.pnas.org/cgi/doi/10.1073/pnas.0605293103

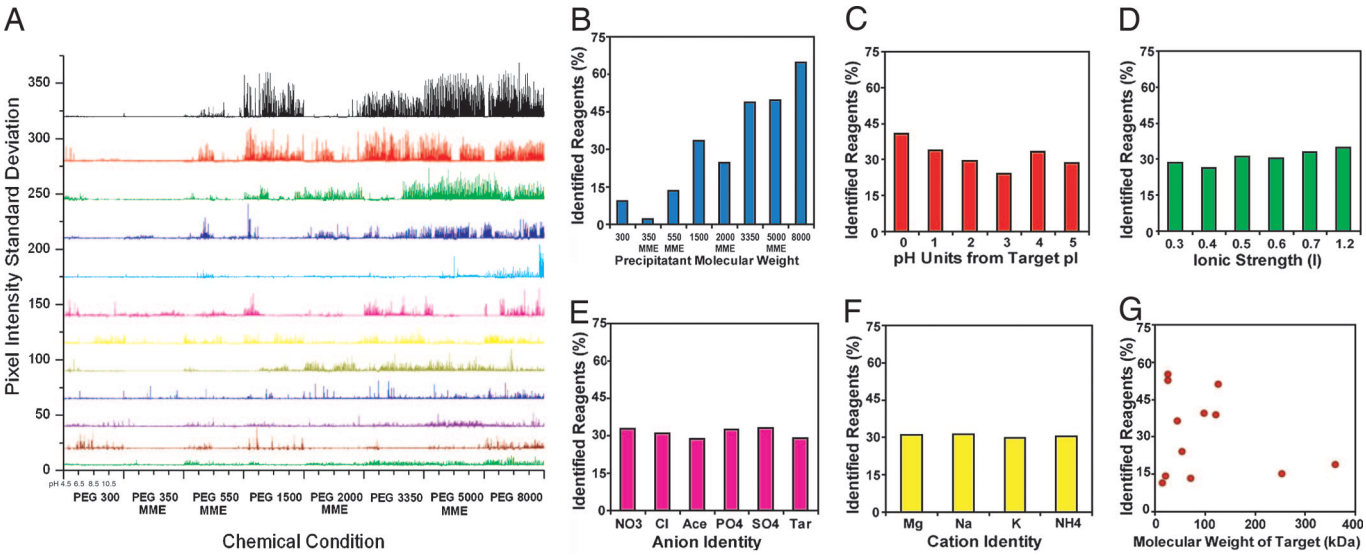

Fig. 1. Solubility information for protein targets. (*A*) Solubility screening results for 12 protein targets. Pixel intensity standard deviation represents the amount of protein aggregation seen in response to each reagent. The proteins are displayed from top to bottom in the order of decreasing protein aggregation: bR D85S, bR, Cbb3, AlaRS, Fis1, P450 1–12G, SMC/ScpA, P2X, AMG, VCP/Vimp, Tf/TfR, and 19S Lid. The solubility screening results are grouped by precipitating agent and are further subdivided by buffering agent. See *Materials and Methods* for a list of the reagents screened. (*B*) Classification of identified reagents by the molecular weight of the precipitating agent. (*C*) Classification of identified reagents by the deviation from the pI of the protein targets. (*D*) Classification of identified reagents by the ionic strength of the solution. (*E*) Classification of the identified reagents by the anion component of the reagent. The anions acetate and tartrate are abbreviated as Ace and Tar, respectively. (*F*) Classification of the identified reagents by the cation component of the reagent. (*G*) Comparison of the target molecular weight and the identified reagents for each target. For *B*–*G*, the percentage of identified reagents is normalized by the number of reagents screened in each category.

of 448 reagents composed of unique precipitant, buffer, and salt combinations. For each reagent, protein phase behavior was explored by sampling protein solubility at six different protein and precipitant concentrations across the phase diagram for a total of 2,688 solubility experiments per target. The ability of each reagent to manipulate protein solubility was quantified by the amount of protein aggregation observed when the protein was introduced to the reagent. Reagents that caused protein aggregation above a threshold level were considered to be potential crystallizing reagents for that target. The solubility screening across chemical and phase space identified between 51 and 246 potential crystallizing reagents for each of the targets.

Trends in the solubility screening results indicate that protein phase behavior was predominately controlled by the precipitat-

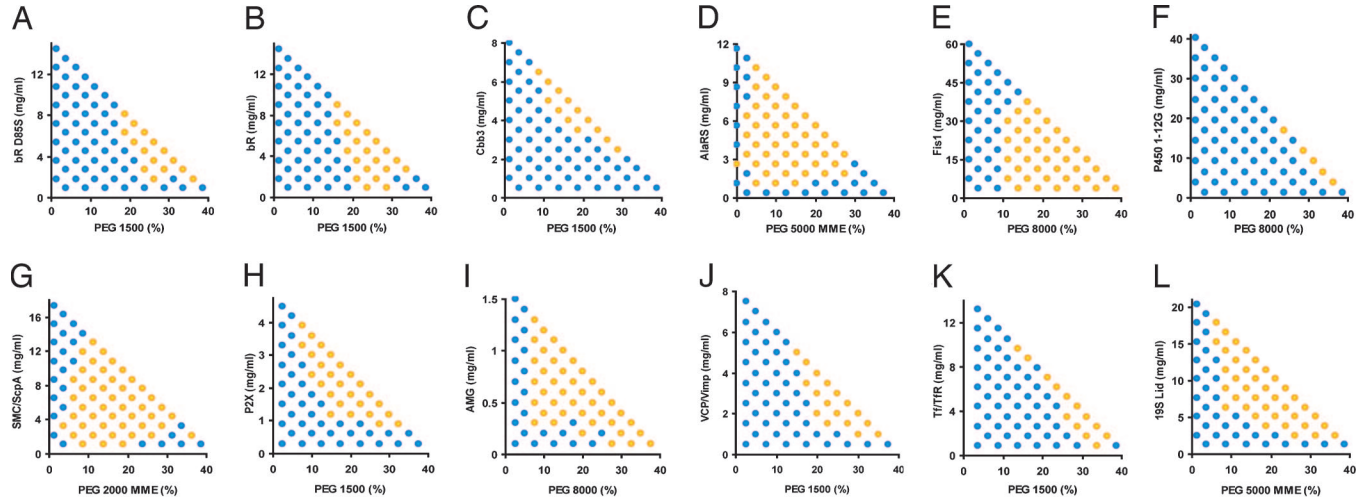

Fig. 2. Phase behavior characterization for targets. One complete phase diagram is shown for each target. (*A*) bR D85S with 0.125 M potassium acetate, 0.1 M sodium citrate (pH 6.5), and PEG 1500. (*B*) bR with 0.125 M ammonium chloride, 0.1 M sodium acetate (pH 4.5), and PEG 1500. (*C*) Cbb3 with 0.075 M sodium acetate, 0.1 M sodium citrate (pH 6.5), and PEG 1500. (*D*) AlaRS with 0.1 M magnesium sulfate, 0.1 M sodium citrate (pH 5.5), and PEG 5000 MME. (*E*) Fis1 with 0.1 M ammonium acetate, 0.1 M Tris·HCl (pH 8.5), and PEG 8000. (*F*) P450 1–12G with 0.2 M ammonium sulfate, 0.1 M imidazole (pH 7.5), and PEG 8000. (*G*) SMC/ScpA with 0.05 M magnesium sulfate, 0.1 M sodium citrate (pH 5.5), and PEG 2000 MME. (*H*) P2X with 0.3 M sodium acetate, 0.1 M Hepes (pH 7.5), and PEG 1500. (*I*) AMG with 0.5 M sodium chloride, 0.1 M Tris·HCl (pH 8.5), and PEG 8000. (*J*) VCP/Vimp with 0.4 M ammonium acetate, 0.1 M sodium citrate (pH 6.5), and PEG 1500. (*K*) Tf/TfR with 0.2 M ammonium sulfate, 0.1 M Hepes (pH 7.5), and PEG 1500. (*L*) 19S Lid with 0.1 M ammonium chloride, 0.1 M sodium citrate (pH 5.5), and PEG 5000 MME. Each phase diagram screened protein solubility at 72 different precipitant and protein concentrations. The blue points represent concentrations where the protein is soluble, and the yellow points represent concentrations where the protein is insoluble.

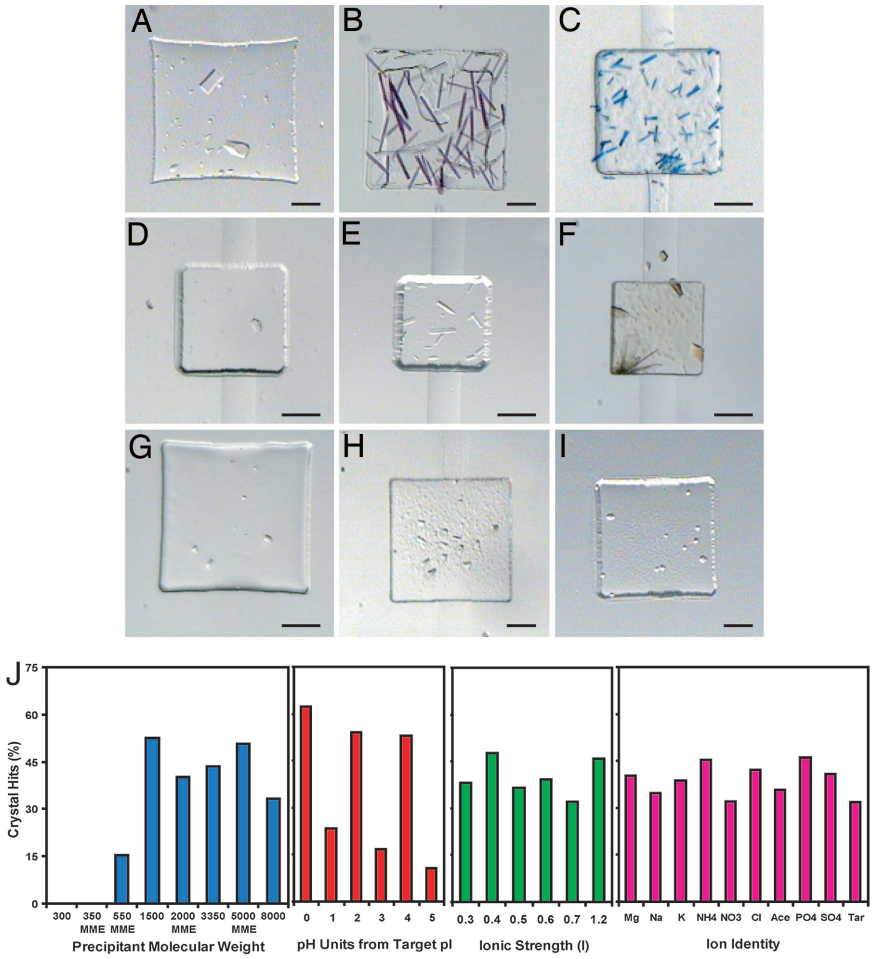

Fig. 3. Crystallization by using phase behavior information. Nine of the 12 targets were crystallized in free interface diffusion screening devices. (*A*) VCP/Vimp rhombohedral crystals were grown in 0.44 M sodium chloride, 0.1 M sodium citrate (pH 6.0), and 6% PEG 1500. (*B*) bR rod crystals were grown in 0.25 M ammonium chloride, 0.1 M sodium acetate (pH 4.5), and 35% PEG 1500. (*C*) bR D85S rod crystals were grown in 0.125 M potassium acetate, 0.1 M sodium citrate (pH 6.5), and 35% PEG 1500. (*D*) Fis1 crystals were grown in 0.1 M ammonium acetate, 0.1 M Tris·HCl (pH 8.5), and 20% PEG 8000. (*E*) 19S Lid rectangular prism crystals were grown in 0.15 M sodium acetate, 0.1 M sodium citrate (pH 5.5), and 15% PEG 8000. (*F*) P450 1–12G plate crystals were grown in 0.28 M ammonium sulfate, 15% 1,3-propanediol, 0.1 M imidazole (pH 7.5), and 30% PEG 8000. (*G*) AlaRS crystals were grown in 0.15 M magnesium sulfate, 0.1 M sodium citrate (pH 5.5), and 15% PEG 5000 MME. (*H*) SMC/ScpA crystals were grown in 0.05 M magnesium acetate, 0.1 M sodium citrate (pH 5.5), and 60% PEG 550 MME. (*I*) Cbb3 hexagonal crystals were grown in 0.125 M sodium chloride, 0.1 M sodium citrate (pH 6.5), and 15% PEG 1500. (*J*) Classification of crystal hits by the molecular weight of the precipitating agent in the reagent, the deviation of the reagent from the pI of the protein targets, the ionic strength of the reagent, and the ionic component of the reagent. The percentage of crystal hits is normalized by the number of reagents screened in each category. (Scale bars, 100 μm.)

ing component of the reagent (Fig. 1*B*). The effectiveness of each of the reagent components on protein aggregation was determined by comparing the solubility results of reagents with two of the three components held constant. The precipitants used in the solubility experiments are polyethylene glycol (PEG) polymers with different chain lengths and end groups, giving each PEG polymer unique volume exclusion properties. Since the volume exclusion effect is more significant in longer polymers because of their larger radius of gyration, the longer polymers were used at a lower concentration than the shorter polymers. Polymers of four different chain lengths were examined, and for every target the number of potential reagents identified with longer polymers surpassed the number of reagents identified with shorter polymers. Additionally, a second PEG polymer with a modified monomethyl ether (MME) end group was screened at each polymer length; the MME polymers produced fewer identified reagents at each polymer length. Therefore, increasing the polymer chain length of the precipitating agent increases the protein aggregation response, and the polymer chemical composition also influences protein aggregation.

The solubility screening results also show that reagents with a pH value in the vicinity of the theoretical isoelectric point (pI) of the targets were identified as potential reagents with a slightly higher frequency than reagents that deviated from the target pI values (Fig. 1*C*). This increased identification of reagents is consistent with the reduced intermolecular electrostatic repulsion of proteins near their pI. The variation in the identified reagents at different pH values was moderate in comparison with the variations seen for precipitant composition. The ionic strength of the salt solutions used in the solubility screening exhibited the expected trend of increased identified reagents at higher ionic strengths (Fig. 1*D*). Although ionic strength had a small influence on the identified reagents, no trends were observable for the ionic composition of the reagents (Fig. 1*E-F*). The ions are displayed by increasing protein aggregation strength based on the Hofmeister series, and little variation in the identified reagents is seen for the cation or anion components of the reagent (15). A trend is also evident between the decreasing molecular weight of the target and an increasing number of identified reagents (Fig. 1*G*).

Protein phase behavior was further characterized by the generation of complete phase diagrams for a subset of the reagents identified during the solubility screening. Empirically determined solubility boundaries allow for the selection of precipitant and protein concentrations that maximize the chance of successful crystallization by excluding areas of phase space that lie far into the precipitation or soluble regions. The complete phase diagrams were produced by combining protein and reagent at 72 different protein and precipitating agent concentrations across the phase diagram and measuring protein aggregation at each position (Fig. 2). Positions where the protein aggregated above a threshold level were classified as insoluble, and positions where the protein did not aggregate above a threshold value were classified as soluble. The phase diagrams were used to design free interface diffusion experiments that target the solubility boundary of the protein with each reagent. For example, the phase diagram shown in Fig. 2*A* suggests that targeting the position corresponding to 6 mg/ml bR D85S and 20% (wt/vol) PEG 1500 would promote crystallization. A free interface diffusion experiment targeting this position requires combining 12 mg/ml bR D85S with 40% (wt/vol) PEG 1500 at a 1:1 protein to reagent ratio. As the free interface diffusion experiment proceeds, the trajectories for each solution will evolve to reach the desired position and promote protein crystallization (see figure 3 in ref. 16 for details). Customized crystallization conditions were designed by using this technique for the specific reagents identified for each of the targets.

Crystallization experiments were carried out with the individualized rational screens by using a redesigned free interface diffusion screening device (16). Each of the crystallization conditions was tested against the protein at five different mixing ratios to completely sample the solubility boundary of the associated phase diagram (see *Materials and Methods* for details). Free interface diffusion experiments with the rational screens resulted in a 75% crystallization success rate for the proteins, whereas previous crystallization attempts in the labs of collaborators failed to identify crystallization conditions for the majority of the samples (Fig. 3). For the successfully crystallized proteins, between 12% and 79% of the reagents screened produced crystals. The targets were bimodal in their crystallization success rates; the majority of the targets crystallized for a small subset of the reagents screened while the remaining targets crystallized for the majority of the reagents screened.

The crystallization results show that the crystal hits fall within a well defined region of precipitant and pH (Fig. 3*J*). Among the precipitants used for crystallization experiments, more crystal hits occurred with larger precipitants, and no crystal hits were identified for the smallest precipitants. In contrast to the observed protein aggregation trends, more crystal hits were identified with the chemically modified MME precipitants for the larger precipitants. Although the variation in pH was larger, more crystal hits were identified from reagents near the pI value of the targets. No trend is observed in the number of crystal hits and the ionic strength of the reagent. As was observed for the protein aggregation results, the variation in crystal hits based on the ion identity of the reagent is small with no apparent trends.

Various crystal morphologies appeared in response to different reagents, including rectangular prism crystals, rhombohedral crystals, hexagonal crystals, rod crystals, plates, needles, dendrites, and spherulites. Optimization of the initial crystallization results with additional free interface diffusion experiments improved crystal size and morphology. The best crystallization conditions for each target were transported to larger experimental formats to generate crystals large enough for diffraction analysis (Fig. 4). The crystallization conditions were translated to scale-up diffraction devices (17), vapor diffusion format, or microbatch format with a 67% success rate. Successful translation to larger formats was also clearly correlated with the crystal quality attainable in the smaller format crystallization experiments.

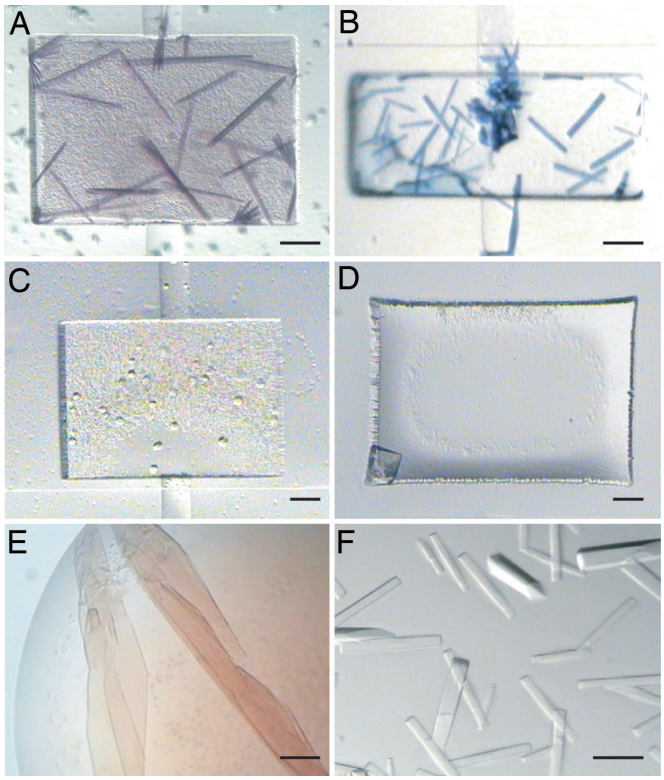

Fig. 4. Larger-format crystals for diffraction analysis. Initial hits for six of the nine targets were transported to a larger-scale growth format. (*A*) bR rod crystals were grown in scale-up diffraction devices with 0.1 M potassium sodium tartrate, 0.1 M sodium acetate (pH 4.5), and 35% PEG 1500. (*B*) bR D85S rod crystals were grown in scale-up diffraction devices with 0.1 M sodium nitrate, 0.1 M sodium citrate (pH 6.5), and 25% PEG 1500. (*C*) Cbb3 hexagonal crystals were grown in scale-up diffraction devices with 0.15 M ammonium acetate, 0.1 M sodium citrate (pH 5.5), and 30% PEG 1500. (*D*) VCP/Vimp rhombohedral crystals were grown in scale-up diffraction devices with 0.4 M sodium chloride, 0.1 M sodium citrate (pH 6.5), and 10% PEG 1500. (*E*) P450 1–12G plate crystals were grown by using vapor diffusion with 0.3 M ammonium sulfate, 0.1 M imidazole (pH 7.8), and 28% PEG 8000. (*F*) 19S Lid rectangular prism crystals were grown in microbatch with 0.175 M sodium acetate, 0.1 M sodium citrate (pH 5.5), and 14% PEG 8000. (Scale bars, 100 μm.)

Diffraction experiments were performed on the crystals grown in larger formats to evaluate the quality of the crystals. Of the six crystals successfully transported to larger formats for diffraction studies, 67% of these crystals produced diffraction data (Fig. 5). This corresponds to a 33% overall success rate of starting with purified protein and finishing with diffraction-quality crystals. The membrane proteins diffracted to between 6.7 Å and 16 Å, and the metabolic protein diffracted to 3.7 Å with a centered monoclinic unit cell of dimensions $a = 19.9$ Å, $b = 62.2$ Å, $c = 188.7$ Å, $\alpha = 90°$, $\beta = 118.91°$, and $\gamma = 90°$.

A point of concern is that although this method is highly successful at generating diffraction-quality crystals, the diffraction resolution has not been high enough to solve the structures. In contrast, the PSI has been quite successful in transitioning from diffraction-quality crystals to solved structures. Reasons for this discrepancy could include the inherent crystallization difficulty of the targets we attempted, quality control on the protein production side, and a lack of target optimization by the systematic truncation of floppy subunits. Additionally, further optimization of the crystal growth conditions by using tools such as small-molecule additive screening or temperature control

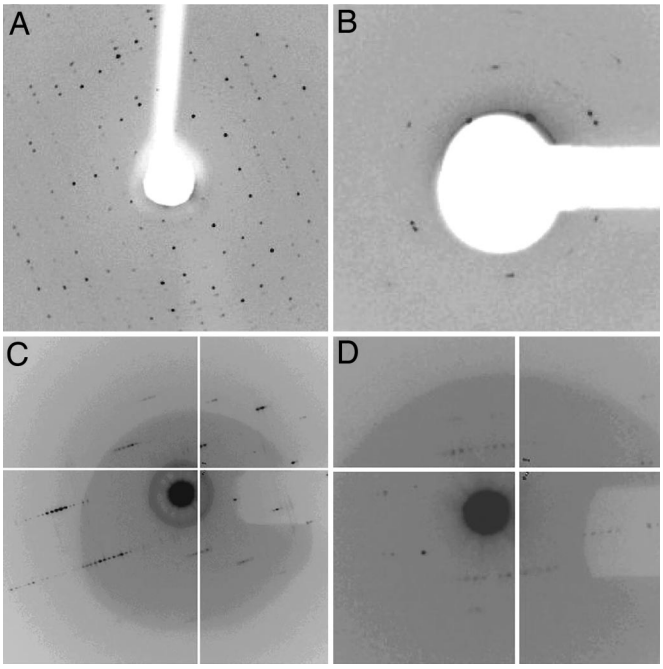

Fig. 5. Diffraction images of larger-format crystals. (*A*) P450 1–12G crystals were harvested by using 25% ethylene glycol as a cryoprotectant and diffracted to 3.7 Å. The unit cell is centered monoclinic with dimensions $a = 219.9$ Å, $b = 62.2$ Å, $c = 188.7$ Å, $\alpha = 90°$, $\beta = 118.91°$, and $\gamma = 90°$. (*B*) Diffraction data for Cbb3 crystals were collected at room temperature by using scale-up diffraction devices, and the crystals diffracted to 14.5 Å. (*C*) Diffraction data for bR D85S crystals were collected through scale-up diffraction devices by using 20% glycerol as a cryoprotectant, and the crystals diffracted to 6.7 Å. (*D*) bR crystals grown in scale-up diffraction devices were harvested by using 15% PEG 1500 as a cryoprotectant and diffracted to 16 Å.

could improve the diffraction resolution of the crystals. The crystal optimization efforts were directly proportional to the limited amount of material provided for each of the targets.

Our success rates of 75% for crystallization and 33% overall rate of producing diffraction-quality crystals from purified protein are roughly double those of the PSI, which are 38% and 18%, respectively (http://targetdb.pdb.org/statistics/TargetStatistics.html). One must, however, also take into account the relatively small sample size in the present survey ($N = 12$) compared with the large number ($N \sim 10{,}000$) tested by the PSI, which leads to a lower statistical significance in our observed rates. We have tried to mitigate this effect by choosing protein targets that are well above average in their crystallization difficulty; the vast majority of our targets failed conventional crystallization attempts. The size of the present data set notwithstanding, we believe the evidence is strong enough to suggest that microfluidic crystallization tools should become incorporated in large-scale structural genomics efforts.

In conclusion, the rational phase diagram-based crystallization strategy presented in this article was successfully used to crystallize diverse and challenging proteins. The use of solubility information to design customized crystallization screens doubled the crystallization success rate over traditional screening techniques and increased the production of diffraction-quality crystals. Microfluidic devices such as these consume small amounts of protein, are inexpensive, and are amenable to use in high-throughput crystallization efforts.

Materials and Methods

Protein Preparation. Protein samples were provided by the following collaborators: 98-kDa *Aquifex aeolicus* alanyl-tRNA synthetase (AlaRS) at 15 mg/ml was from Manal Swairjo (The Scripps Research Institute); 22-kDa human amelogenin (AMG) at 2 mg/ml was from Stefan Habelitz (University of California, San Francisco); 27-kDa *Halobacteria* bacteriorhodopsin (bR) and bacteriorhodopsin mutant D85S (bR D85S) at 18 mg/ml were from Marc Facciotti and Lee Hood (Institute for Systems Biology); 126-kDa *Rhodobacter sphaeroides* cytochrome cbb3 (Cbb3) at 10 mg/ml was from Michael Merckel (University of Helsinki); 16-kDa *Saccharomyces cerevisiae* Fis1 at 60 mg/ml was from Takumi Koshiba and David Chan (California Institute of Technology); 360-kDa *Saccharomyces cerevisiae* proteasome 19S Lid particle (19S Lid) at 25 mg/ml was from Xavier Ambroggio, Douglas Rees, and Raymond Deshaies (California Institute of Technology); 45-kDa *Mus musculus* P2X at 6 mg/ml was from Pavel Strop and Axel Brunger (Stanford University); 54-kDa heme domain of *Bacillus subtilis* cytochrome P450 mutant 1–12G (P450 1–12G) at 30 mg/ml was from Matthew Peters, Peter Meinhold, and Frances Arnold (California Institute of Technology); 123-kDa *Aquifex aeolicus* SMC/ScpA complex at 22 mg/ml was from Scott Gradia and James Berger (University of California, Berkeley); 72-kDa human tranferrin/transferrin receptor mutant complex (Tf/TfR) at 27 mg/ml was from Anthony Giannetti and Pamela Bjorkman (California Institute of Technology); and 254-kDa *Rattus norvegicus* VCP-97/Vimp complex (VCP/Vimp) at 10 mg/ml was from Byron DeLaBarre and Axel Brunger (Stanford University).

Solubility Screening and Phase Diagram Generation. Solubility experiments were performed by using a microfluidic formulator device developed by Hansen *et al.* (2004). Device fabrication, automation, experimental setup, and data acquisition were previously described (13). The formulator device was used to create 448 unique reagents for solubility screening by systematically combining 14 salt solutions, 4 buffering agents, and 8 precipitating agents. The salt solutions used were 4 M ammonium acetate, 3 M sodium acetate, 5 M ammonium chloride, 5 M sodium chloride, 2 M potassium sodium tartrate, 4 M ammonium sulfate, 7 M sodium nitrate, 2 M magnesium acetate, 2 M magnesium chloride, 2 M magnesium sulfate, 5 M potassium acetate, 3 M potassium chloride, 2 M potassium phosphate, and 4 M sodium phosphate. The buffering agents used were 1 M sodium acetate (pH 4.5), 1 M sodium citrate (pH 6.5), 1 M Tris·HCl (pH 8.5), and 1 M 3-(cyclohexylamino)-1-propanesulfonic acid (pH 10.5). The precipitating agents used were 100% (wt/vol) PEG 300, 100% (wt/vol) PEG 350 MME, 100% (wt/vol) PEG 550 MME, 50% (wt/vol) PEG 1500, 50% (wt/vol) PEG 2000 MME, 50% (wt/vol) PEG 3350, 50% (wt/vol) PEG 5000 MME, and 50% (wt/vol) PEG 8000. Salt solutions and precipitating agents were used near the maximal solubility and viscosity levels of each species. Each of the reagents was tested against the protein targets at six different protein and precipitant concentrations across the boundary of the phase diagram while holding the salt solution and buffering agent at a fixed level. The salt solutions were used at final concentration of 2.5% of the stock solutions (0.05–0.175 M; see above), and the buffering agents were used at a final concentration of 0.1 M. The six points tested were (*i*) 80% precipitating agent and 2.5% protein, (*ii*) 67.5% precipitating agent and 15% protein, (*iii*) 52.5% precipitating agent and 30% protein, (*iv*) 37.5% precipitating agent and 45% protein, (*v*) 22.5% precipitating agent and 60% protein, and (*vi*) 7.5% precipitating agent and 75% protein. A total of 2,688 solubility experiments were performed for each protein target. Protein aggregation was quantified by imaging the protein in solution with each reagent using a charge-coupled device camera, calculating the pixel intensity standard deviation, and subtracting the background pixel intensity standard deviation of the reagent in the absence of protein. Reagents that caused the protein to aggregate above 3 pixel intensity standard deviation

units for at least one of the six points tested were classified as potential crystallization reagents. For 3.3% of the images, the pixel intensity standard deviation value was negative because of errors in the formulator device, and for these measurements the pixel intensity standard deviation was set to zero.

Complete phase diagrams were generated for a subset of the crystallizing reagents identified with the solubility screening. For each phase diagram, the reagent was combined with the protein at 72 different precipitant and protein concentrations. The protein concentration was tested between 5% and 80%, and the precipitant concentration was tested between 2.5% and 77.5%. Again, buffering agent and salt solution concentrations were held constant throughout the phase diagram at the concentrations listed above for the solubility screening. Protein aggregation was measured at each point as described above. Positions on the phase diagram that caused the protein to aggregate above 3 pixel intensity standard deviation units were classified as insoluble, and positions below 3 were classified as soluble.

Crystallization Experiments and Device Fabrication. Initial crystallization experiments were performed by using a modified version of the microfluidic free interface diffusion screening device (16). The screening device design was modified to perform five free interface diffusion experiments per reagent instead of three. The protein:reagent mixing ratios used were 1:4, 1:2, 1:1, 2:1, and 4:1, with a total reaction volume of 25 nl per free interface diffusion experiment. One screening device was used to test 48 reagents for a total of 240 parallel free interface diffusion experiments. The previous design used a hybrid glass/elastomer device and was modified to consist solely of elastomer to facilitate faster fabrication. The devices were fabricated by using multilayer soft lithography (18). Two negative master molds were fabricated for the control structures and for the flow structures with photoresist by using conventional lithography techniques. The 20-μm-thick control structures were fabricated by spinning photoresist (MicroChem SU-8 2025) onto a silicon wafer at 3,000 rpm for 75 s and patterned by using a negative high-resolution transparency mask printed at 101.5% of the desired device size. For the flow structures, the 13-μm-thick reaction channels were fabricated by spinning photoresist (Shipley SPR 220-7) onto a second silicon wafer at 1,300 rpm for 70 s and patterned by using a positive high-resolution transparency mask. The reaction channels were rounded by annealing at 180°C for 1 h. Next, the 45-μm-thick reaction chambers were fabricated on top of the reaction channels by spinning photoresist (MicroChem SU-8 50) onto the second silicon wafer at 2,000 rpm for 45 s and patterned by using a negative high-resolution transparency mask.

Elastomeric devices were created by pouring silicone elastomer (General Electric RTV 615; 5 parts A:1 part B) onto the flow structures to 1-cm thickness and by spinning elastomer (20 parts A:1 part B) at 2,000 rpm for 60 s onto the control structures for a thickness of 30 μm. The flow layer and the control layer were partially cured at 80°C for 60 min and 40 min, respectively, before the flow layer was peeled off of the flow mold and aligned to the control layer. After the aligned device was cured for an additional 1.5 h, the device was removed from the control mold and the control and flow ports were punched with 20- and 14-gauge punching tools (Technical Innovations), respectively. A blank layer of elastomer (20 parts A:1 part B) was spun at 2,000 rpm for 60 s on a blank silicone wafer and partially cured for 30 min at 80°C. The aligned device was bonded onto the blank layer overnight at 80°C, and the device was completed by removal from the blank silicone wafer and placement on a glass microscope slide (Corning).

The crystallization experimental setup is described in ref. 16. Crystal hits were verified by using IZIT protein stain, the crush test, or diffraction analysis. Crystal hits were transported to microfluidic scale-up diffraction devices, vapor diffusion format, or microbatch format for diffraction experiments. Device fabrication and experimental setup with the scale-up diffraction device is described in ref. 17. Scale-up diffraction devices were incubated at room temperature up to 2 weeks, and cryoprotectant was introduced by diffusion 24 h before flash-freezing the crystals in the devices. For vapor diffusion experiments, 1 μl of protein was combined with 1 μl of reagent and suspended over 500 μl of reagent and incubated at room temperature up to 2 weeks. For microbatch experiments, a layer of paraffin oil was place over the microbatch wells, and 1 μl of protein was combined with 1 μl of reagent under the oil and incubated at room temperature up to 2 weeks. For vapor diffusion and microbatch experiments, the crystals were looped from the drops and through cryoprotectant before flash-freezing in liquid nitrogen.

Diffraction Studies. Diffraction data for Cbb3 were collected at station 11.1 of the Stanford Linear Accelerator Center (Stanford University), at an incident wavelength of 1.0 Å with a 15-s exposure and 1° oscillation. Diffraction data for bR and bR D85S were collected at station 8.3.1 of the Advanced Light Source (Lawrence Berkeley National Laboratory), at an incident wavelength of 1.0 Å with a 20-s exposure and 1° oscillation. Diffraction data for P450 1–12G were collected on an R-axis IV (California Institute of Technology) at an incident wavelength of 1.54 Å with a 30-min exposure and 1° oscillation.

We thank the laboratories of Frances Arnold, David Chan, Douglas Rees, Raymond Deshaies, Pamela Bjorkman, Axel Brunger, James Berger, Stefan Habelitz, Michael Merckel, Lee Hood, and Manal Swairjo for generously providing the materials used in this work. This work was supported by the National Institute of Health Director's Pioneer Award.

1. Carter CW, Jr, Carter CW (1979) *J Biol Chem* 254:12219–12223.
2. Jancarik J, Kim S-H (1991) *J Appl Crystallogr* 24:409–411.
3. Carbonnaux C, Ries-Kautt M, Ducruix A (1995) *Protein Sci* 4:2123–2128.
4. Ewing F, Forsythe E, Pusey M (1994) *Acta Crystallogr D* 40:424–428.
5. Forsythe EL, Judge RA, Pusey ML (1999) *J Chem Eng Data* 44:637–640.
6. Gaucher J-F, Ries-Kautt M, Reiss-Husson F, Ducruix A (1997) *FEBS Lett* 401:113–116.
7. Odahara T, Ataka M, Katsura T (1994) *Acta Crystallogr D* 30:639–642.
8. Ries-Kautt MM, Ducruix AF (1989) *J Biol Chem* 264:745–748.
9. Saridakis E, Chayen NE (2003) *Biophys J* 84:1218–1222.
10. Saridakis EEG, Shaw Stewart PD, Lloyd LF, Blow DM (1994) *Acta Crystallogr D* 50:293–297.
11. Sauter C, Lorber B, Kern D, Cavarelli J, Moras D, Giege R (1999) *Acta Crystallogr D* 55:149–156.
12. Yoshizaki I, Nakamura H, Fukuyama S, Komatsu H, Yoda S (2004) *Ann NY Acad Sci* 1027:28–47.
13. Hansen CL, Sommer MOA, Quake SR (2004) *Proc Natl Acad Sci USA* 101:14431–14436.
14. Sommer MOA, Larsen S (2005) *J Synchrotron Radiat* 12:779–785.
15. Hofmeister F (1888) *Arch Exp Pathol Pharmakol* 24:247–260.
16. Hansen CL, Skordalakes E, Berger JM, Quake SR (2002) *Proc Natl Acad Sci USA* 99:16531–16536.
17. Hansen CL, Classen S, Berger JM, Quake SR (2006) *J Am Chem Soc* 128:3142–3143.
18. Unger MA, Chou H, Thorsen T, Scherer A, Quake SR (2000) *Science* 288:113–116.